



OPEN

Ball-milling synthesized $\text{Bi}_2\text{VO}_{5.5}$ for piezo-photocatalytic assessment

Manish Kumar¹, Rahul Vaish¹, Imen Kebaili², Imed Boukhris², Hyeong Kwang Benno Park³, Yun Hwan Joo³, Tae Hyun Sung³ & Anuruddh Kumar⁴✉

The mechanochemical ball milling followed by heating at 650 °C for 5 h successfully produced the single-phase $\text{Bi}_2\text{VO}_{5.5}$ powder. Catalytic activity for methylene blue dye degradation was investigated. Raman spectroscopy and X-ray diffraction were used to confirm the phase formation. The sample's charge carrier transportation behavior was ascertained using time-dependent photocurrent analysis. The piezo-photocatalysis experiment yielded a 63% degradation efficiency for the ball-milled $\text{Bi}_2\text{VO}_{5.5}$ sample. The pseudo-first-order kinetics of the piezo-photocatalytic dye degradation are discerned, and the significant k value of 0.00529 min^{-1} is achieved. The scavenger test declares the h^+ radical is the predominant active species during the piezo-photocatalysis experiment. *Vigna radiata* seeds were used in a phytotoxicity test to evaluate the germination index. The mechanochemical activation method facilitates reactions by lowering reaction temperature and time. The effect of improved piezo-photocatalytic efficiency on the ball-milled $\text{Bi}_2\text{VO}_{5.5}$ powder is an unexplored area, and we have attempted to investigate it. Here, ball-milled $\text{Bi}_2\text{VO}_{5.5}$ powder achieved improved dye degradation performance.

Currently, the rapid rate of industrialization has pushed human society into a new era where the conservation of the environment is a major concern. People have started to realize the need for environmental conservation by finding better ways to address environmental damage¹. Organic pollutants that are very frequently employed in food, pharmaceutical, printing, dyeing, and other industries include colors and antibiotics². Organic dyes are a significant component of industrial wastewater as textile industries discharge them in large quantities directly into aquatic sources causing serious environmental risks and are harmful to human health as well³. Organic pollutants being carcinogenic and poisonous deteriorate aquatic, animal, and human health⁴. Numerous studies have been conducted and published in the literature to create standard methods for removing pollutants from industrial wastewater^{5,6}. Conventional methods of water purification, such as coagulation, adsorption, ultra-filtration, and microbial degradation, have been the norm for treating wastewater until recently⁷. However, these techniques have the flaw of having poor removal efficiency, the secondary pollutant that needs further treatment, and difficulty in eliminating contaminants with low concentrations^{7,8}. Therefore, it became vital to create efficient and ecologically acceptable processes to break down these organic contaminants.

Multiple physical, chemical, and biological processes are now used for the treatment of textile wastewater⁹. Tested and affordable technology is photocatalysis and piezocatalysis^{10,11}. They are considered green alternatives due to their potential to be environment friendly and eliminate organic contaminants from aqueous solutions with high efficiency^{4,12}. In semiconductor photocatalysis, improvement of the photocatalyst is required to enhance their abilities to absorb light while facilitating the separation of different charge carriers^{13,14}. Semiconductor photocatalysts showed remarkable potential in photocatalysis because of their unique band structures, mobility, and excellent separation of photogenerated charge carriers¹⁵. Benefits of photocatalysis include the ability to oxidize toxins at room temperature at low concentrations, the reduction of secondary pollutants, low cost, and non-toxicity which makes it appropriate for the degradation of the contaminants^{16,17}. Anatase TiO_2 is currently the most preferred photocatalyst due to its higher oxidizing power, lower price, and excellent chemical stability^{18,19}. Owing to its broad bandgap (3.20 eV) and the relatively small lifespan of photo-induced carriers, TiO_2 has poor quantum efficiency since it can only absorb the UV part of the sun's rays^{1,18}. Therefore, it's critical to create an effective

¹School of Engineering, Indian Institute of Technology Mandi, Mandi, Himachal Pradesh 175005, India. ²Department of Physics, Faculty of Science, King Khalid University, P.O. Box 9004, Abha, Saudi Arabia. ³Department of Electrical Engineering, Hanyang University, 222, Wangsimni-ro, Seongdong-gu, Seoul 04763, Korea. ⁴Center for Creative Convergence Education, Hanyang University, 222, Wangsimni-ro, Seongdong-gu, Seoul 04763, Korea. ✉email: anuruddh07@hanyang.ac.kr

visible-light-active photocatalyst. In addition to photocatalysis, ultrasonic vibration-induced piezocatalysis can also be utilized alone or in combination for wastewater treatment^{20,21}. There has been an immense search to create new photocatalysts that respond to visible light more effectively. Bi-based semiconductors have garnered considerable attention owing to their novel characteristics and easy availability of raw materials^{7,22}. In presence of the hybridized Bi (6s) and O (2p) valence bands, many oxides containing Bi³⁺ have photocatalytic characteristics²³. As new photocatalytic materials, bismuth-based substances such as BiVO₄, Bi₂WO₆, Bi₂MoO₆, CaBi₂O₄, BiNbO₄, and Bi₂VO_{5.5} have been reported^{1,24–27}. The bismuth-based oxides, like bismuth vanadate, possess spectacular features such as corrosion resistance, nontoxicity, ferroelasticity, and ionic conductivity^{28,29}. In contrast to the majority of ferroelectric materials, bismuth vanadate (Bi₂VO_{5.5}, BV) exhibits simultaneous high ionic mobility and polar responses, two properties that are typically incompatible^{30,31}. There are numerous applications for it, including catalysts, solid electrolytes, gas sensors, and positive electrode materials for lithium rechargeable batteries^{32–34}. Bi₂VO_{5.5} can be produced using several techniques, including sol–gel, co-precipitation, solid-state reaction, and microwave^{33,35,36}. Piezoresponsive behavior is a result of the non-centrosymmetric orthorhombic structure of BV^{37,38}. The material underwent spontaneous polarization due to discrete stable polarization that was induced by the non-centrosymmetric unit cell³⁹. The resulting surface polarization leads to band bending and space charge regions³⁹. The standard formula for Bi₂VO_{5.5} is (Bi₂O₂)²⁺(A_{n–1}B_nO_{3n+1})^{2–}, where B stands for hexa-, tetra-, and pentavalent ions, n for the number of perovskite blocks squeezed between layers of Bi₂O₂, and A for di-, tri-, and mono-valent ions^{40,41}. BV has a layered structure like BiVO₄⁴². Due to its low bandgap, BV is used across a broad visible light absorption range⁴². The traditional ceramic synthesis method requires high temperature and more reaction time⁴³. The Mechanochemical activation method facilitates reactions by lowering reaction temperature and time without changing stoichiometry⁴³. It has been effectively used to speed up compound formation and phase transitions, as well as to improve the physicochemical properties of novel materials^{43,44}. Furthermore, the catalyst's surface area is a crucial component. The catalyst nanoparticle's wide surface area allows for the adsorption of dye molecules that are sufficient for photon capture and electron–hole pair production, which can improve photocatalytic activity^{45,46}. Small particle-size material has been reported to be produced via sol–gel, co-precipitation, microwave, and mechanochemical ball milling (MBM) activated processes^{33,47}. Due to their vast surface area, small particle size is advantageous in enhancing catalytic efficiency⁴⁵. Xie et al.⁴⁸ successfully degraded methylene blue (MB) using Au nanoparticles deposited on Bi₂VO_{5.5} with an efficiency of 85.2%. Jianmin Wang et al. employed a BiVO₄/Bi₂VO_{5.5} nanostructure to degrade methylene orange (MO) by 95% in the presence of visible light⁴². Bi₂VO_{5.5}/Bi₂O₃ composite films were used by Xie et al. to achieve 89.97% MB dye degradation efficiency under simulated sunshine¹.

In a similar spirit, this study presents the findings of a mechanochemical ball milling (MBM) synthesis approach used to produce the intriguing Bi₂VO_{5.5} oxide. Using the MBM synthesis approach to synthesize powdered BiVO₄ sample, we recently reported an 81% degradation efficiency of MB dye using piezo-photocatalysis⁴⁴. Utilizing a Bi₂VO_{5.5} powdered sample that has not been synthesized through a ball mill, we were able to degrade MB dye to attain an efficiency of 82% using piezo-photocatalysis³⁴. Bi₂VO_{5.5} powder made using the MBM process has not yet been investigated for piezo-photocatalytic use. The synergetic effect of photocatalysis and piezocatalysis would attain high disintegration efficiency in a shorter time as compared to the bare photocatalysis and bare piezocatalysis approach. With respect to the meta-stable elevated energy state, the reduction in particle size that occurs during milling causes defects and micro-stress. BV is therefore subjected to post-annealing treatment to eliminate the generated defects^{34,49}. The effect of improved piezo-photocatalytic efficiency on the ball-milled BV powder is an unexplored area, and we have attempted to investigate it here. Dye degradation efficiency and time for treatment would both improve with the ball-milled powder's application in industrial wastewater treatment.

Experimental

Fabrication of Bi₂VO_{5.5} powder. The mechanochemical ball milling (MBM) method is a productive way to create materials with submicron and nanoscale dimensions. Repeated welding and fracture ensure that each material is subjected to a solid-state reaction that results in the final synthesis of powder material. With this technique, submicron-sized powdered material of the right stoichiometry is obtained by alloying the current chemical components. The MBM synthesis method produced BV powder is depicted in Fig. 1. V₂O₅ and Bi₂O₃ oxide powders were combined in a 250 ml tungsten carbide jar according to the stoichiometric molar ratio. In order to mill the material, we used 10 tungsten carbide balls, each of which was 20 mm in diameter. For 17 h duration at 300 rpm speed, a Retsch planetary ball mill (PM100) configuration was employed for the grinding at ambient temperature. After every 30 min, a 5-min break was provided to enable the system to cool. Particle size reduction was further induced during the 26-h wet milling operation at 300 rpm using a specific weight ratio of 1:20:0.5 for the BV powder, yttria stabilized zirconia (YSZ) balls, and ethanol. After separating the YSZ balls, the powders obtained were subjected to a 5-h annealing process at 650 °C to remove any induced defects that may have developed during uninterrupted ball milling. We obtained the ball-milled Bi₂VO_{5.5} (BV) powders after annealing. A distinct Bi₂VO_{5.5} (BiV) that was not subjected ball mill was prepared by grinding using mortar-pestle through utilizing oxide powders of V₂O₅ and Bi₂O₃ in the correct stoichiometric molar ratio to show the comparison in photocatalytic activity. To confirm the Bi₂VO_{5.5} phase, the powders were ground with the aid of a mortar and pestle and then they were calcined at 750 °C for 8 h. The X-ray diffraction method is utilized to establish the BiV phase formed and has been confirmed³⁴. Additionally, a peculiar, not ball-milled Bi₂VO_{5.5} (NBM BiV) was synthesized by combining the oxide powders of V₂O₅ and Bi₂O₃ in the correct molar ratios. The powders were crushed in a mortar and pestle before being calcined for 5 h at a temperature of 650 °C. This was done to understand whether the not ball-milled sample synthesized at a reduced temperature could attain the proper phase formation.

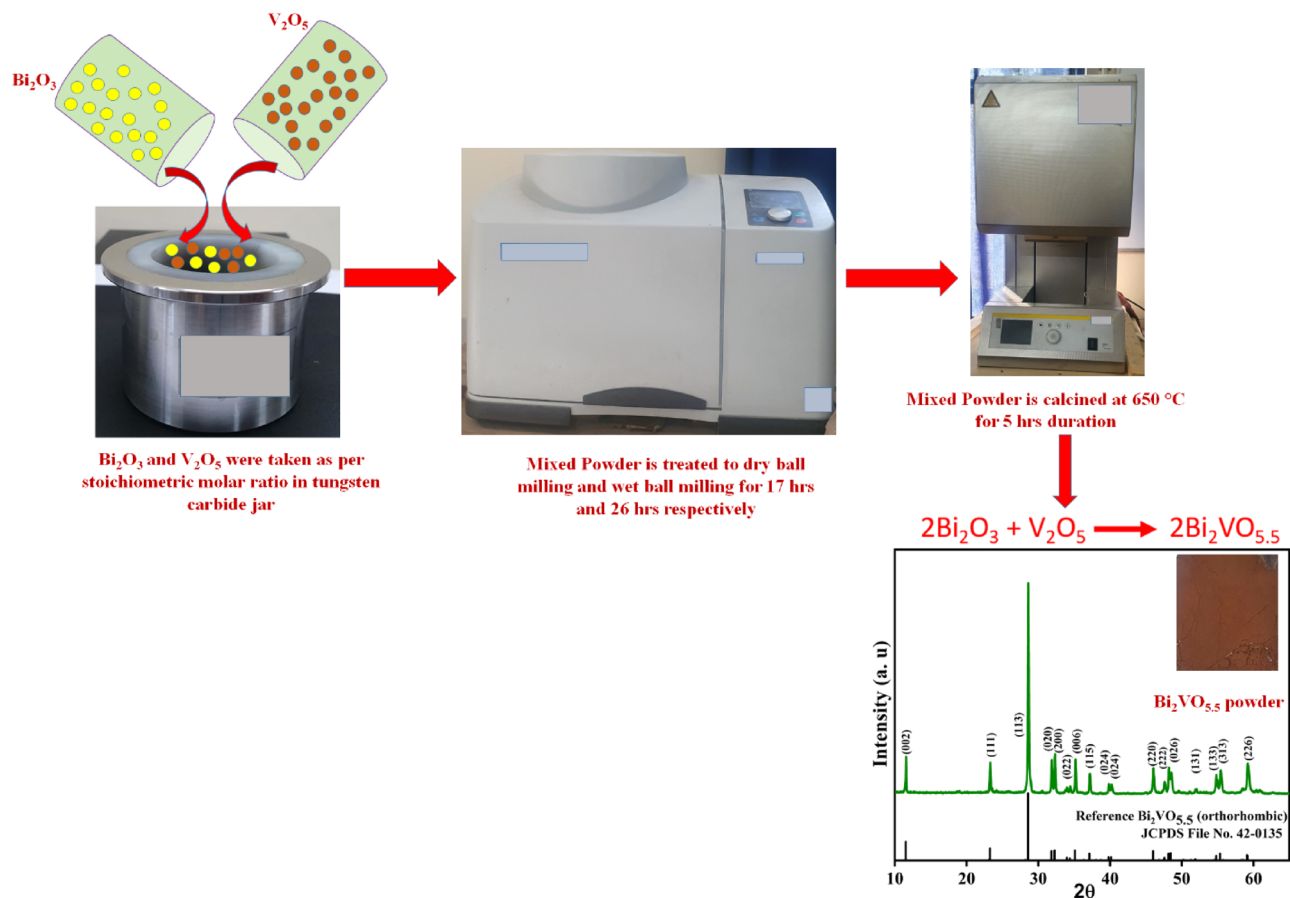


Figure 1. The process involved in making the BV powder.

Sample characterization. The resulting BV powdered samples' phases were determined with the use of the X-ray diffraction technique (XRD, Rigaku diffractometer, Japan). The $2^\circ/\text{min}$ scan rate was applied on the sample powder across a $10\text{--}65^\circ$ 2θ angle range. Raman spectroscopy was utilized to analyze the material's structure and bonding. Using a 10% power 532 nm laser and 600 gratings to scan over the material across the $100\text{--}1300\text{ cm}^{-1}$ range, the Raman spectra were obtained through HORIBA (LabRAM HR Evolution, Japan) spectrometer. The KBr pellets were used as the matrix for a Fourier transform infrared spectroscopy (FTIR) examination performed with a Perkin Elmer spectrum RX I spectrophotometer. Accurate information on the microstructures and surface morphologies of the materials was obtained using a Nova Nano SEM-450 field emission scanning electron microscope (FE-SEM). Energy dispersive spectroscopy (EDS), which is integrated with SEM, was employed to comprehend the compositional elements in the BV sample. X-ray photoelectron spectrometer (Nexsa) equipment was used to evaluate the binding energy and chemical state of the produced BV sample. The UV–visible spectrophotometer (SHIMADZU) was used to evaluate the absorbance peak intensity.

Photocurrent analysis. The generated BV sample's current–time profile was recorded using an electrochemical workstation (AUT86543 Metrohm Autolab B.V.). A platinum wire was used as the counter electrode, and an Ag–AgCl wire was used for both the working and reference electrodes in the three-electrode arrangement. A source of visible light was given by two Havells Company each of 15 W bulbs. To record the photocurrent response, the visible light source went through a few ON and OFF cycles. The used electrolyte was a phosphate-buffered saline solution of 0.1 M concentration. The working electrode was made by mixing 1 mL of ethanol, 5 mg of catalyst, and 20 μL of Nafion solution. After being well mixed together by ultrasonication for 30 min, the resulting catalyst ink was applied as a surface coating on the cleaned glassy carbon electrode with $\sim 10\text{ }\mu\text{L}$ of catalyst ink. Before employing the electrode as the working electrode, it was confirmed that the coat had dried properly.

Bandgap assessments. Diffuse reflectance spectroscopy (DRS) was employed to ascertain the bandgap of the synthesized sample. According to the literature, the direct bandgap was determined by converting the absorption spectra acquired from the DRS into Tauc's plot (a plot between E vs $(\alpha E)^2$)⁵⁰.

Photocatalytic assessment. To evaluate the efficacy of the BV powdered sample in the photocatalytic experiment, we measured the degradation of MB dye in the presence of visible light. Typically, 0.2 g (g) sample

was utilized in the photocatalysis experiment. The adsorption–desorption saturation of the dye was obtained before the start of the photocatalytic evaluation. The first starting dye was swapped out by a new 20 ml dye at a concentration of ~ 5 mg/L when the adsorption equilibrium was acquired. Two light bulbs were used to provide visible light illumination for the BV sample immersed inside the dye solution (Havells company, each of 15W power). A distance of around 12 cm was set between the sample and the incoming light source. Throughout the experiment, the sample was continuously stirred at a 500 rpm speed. The adsorption peak intensity was used to assess the photocatalytic activity. To maintain a constant volume throughout, the test material was carefully replenished back into the beaker after each regular period of acquisition and evaluation of absorbance. For comparison, a photocatalysis evaluation was conducted with the same parameters using a 0.2 g BiV sample that had not been synthesized through a ball mill. According to Eq. (1), the degradation rate percentage of the MB dye was established⁵¹.

$$\% \text{ removal of MB dye} = \frac{C_0 - C}{C_0} \times 100 \quad (1)$$

where C_0 and C stand for the amount of MB dye present before and following the passage of time 't', respectively.

Piezocatalytic assessment. The MB dye degradation in ultrasonic vibration was utilized as a parameter to assess the piezocatalytic efficacy of the powdered BV. Typically, 0.2 grams (g) sample was utilized in the catalysis assessment. The adsorption–desorption saturation of the dye was obtained before the start of the piezocatalysis evaluation. When adsorption saturation is reached, the already used dye is swapped out by a new 20 ml dye at a concentration of ~ 5 mg/L. The BV powder added to the dye solution was then put to ultrasonic vibration received from an ultrasonicator (120 W, 40 kHz). To prevent the dye solution from heating up during ultrasonication, the water in the ultrasonicator was changed after every 15 min because it served as the medium for the process. This experiment was carried out in complete darkness. To maintain a constant volume throughout, the test material was carefully replenished back into the beaker after each regular period of acquisition and evaluation of absorbance. For comparison, a piezocatalysis evaluation was conducted with the same parameters using a 0.2 g BiV sample that had not been synthesized through a ball mill.

Piezo-photocatalysis assessment. The MB dye degradation in the synergetic indulgence of ultrasonic vibration along with visible light illumination was utilized as a parameter to assess the piezo-photocatalytic efficacy of the powdered BV. The BV sample weighing 0.2 g was taken to perform the catalysis evaluation. The adsorption–desorption saturation of the dye was accurately reached before beginning the piezo-photocatalysis evaluation. When adsorption saturation is reached, the already used dye is swapped out by a new 20 ml dye at a concentration of ~ 5 mg/L. The dye solution and BV powder sample were then exposed to both visible light irradiation from two Havells Company bulbs (each with a 15 W power output) and ultrasonic vibration received from an ultrasonicator (120 W, 40 kHz). To prevent the dye solution from heating up during ultrasonication, the water in the ultrasonicator was changed after every 15 min because it served as the medium for the process. To maintain a constant volume throughout, the test material was carefully replenished back into the beaker after each regular period of acquisition and evaluation of absorbance. For comparison, a piezo-photocatalysis evaluation was conducted with the same parameters using a 0.2 g BiV sample that had not been synthesized through a ball mill.

Results and discussion

The XRD scans of the synthesized BV, BiV, and NBM BiV powder samples are shown in Fig. 2. The obtained XRD patterns of BV and BiV show that all the diffracted peaks agree with the orthorhombic $\text{Bi}_2\text{VO}_{5.5}$ standard JCPDS reference file (File No. 42-0135). BV and BiV formed in a single phase without the existence of any secondary phase. $\text{Bi}_2\text{VO}_{5.5}$ phase is present in NBM BiV, although secondary peaks of V_3O_5 , V_2O_5 , V_2O_4 , and Bi_2O_3 are also present at 18.8, 24.2, 26.8, and 27.9 degrees, respectively. In contrast to the 24-h annealing at 1020 K previously described, this study synthesizes single-phase $\text{Bi}_2\text{VO}_{5.5}$ more quickly³¹. The mechanochemically ball milling (MBM) approach produced tiny particles that helped in synthesizing single-phase $\text{Bi}_2\text{VO}_{5.5}$ viable at 650 °C in just 5 h. Further experimental tests are likely to exclude the NBM BiV powdered sample due to the presence of an additional phase and the inability to synthesize the powder using the mortar and pestle method within 5 h at 650 °C.

The Raman bands linked to the fabricated BV sample are shown in Fig. 3a. The Raman spectra were examined between 350 and 1300 cm^{-1} . The major Raman bands were found at the wavelengths 372, 653, 768, 852, and 926 cm^{-1} . These obtained bands are consistent with previously published studies^{9,52}. While the bands at 768 and 653 cm^{-1} reveal the doubly coordinated (V–O–V) oxygen atom, the band observed at 372 cm^{-1} demonstrates the symmetric vibrational mode bending of the V–O bonds^{9,52}. Short-range vibrational V–O bonds are demonstrated by the band obtained at 852 cm^{-1} , while the weak mode at 925 cm^{-1} represents the $\text{V}^{4+}=\text{O}$ unit. The availability of vanadium in the mixed valence state of +4 and +5, causes this weak vibrational mode represented as the $\text{V}^{4+}=\text{O}$ signature⁵².

Material's functional group change is understood by the FTIR spectroscopic analysis of the BV sample shown as in Fig. 3b. In this case, significant IR bands are present at 832, 766, 715, 610, and 529 cm^{-1} . The V–O bond asymmetric stretching is shown by the peak at 832 cm^{-1} while the V–O bond symmetric vibration stretching is shown by the peak at 766 and 715 cm^{-1} ^{153,54}. There are peaks visible at 613, and 529 that show the (O–V–O) vanadate anion deformation^{55,56}.

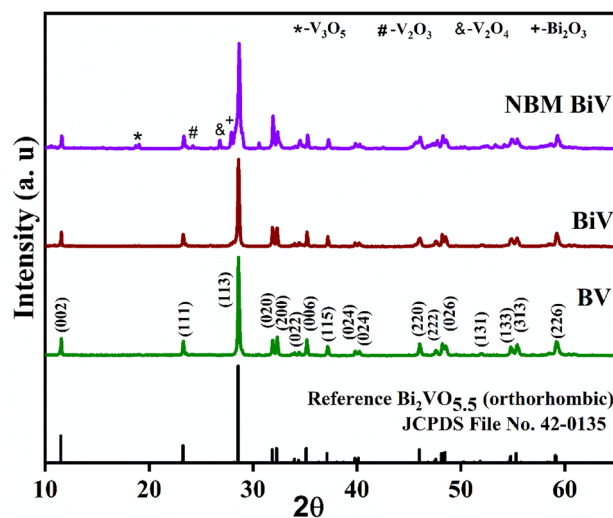


Figure 2. XRD results for BV, BiV, and NBM BiV powders.

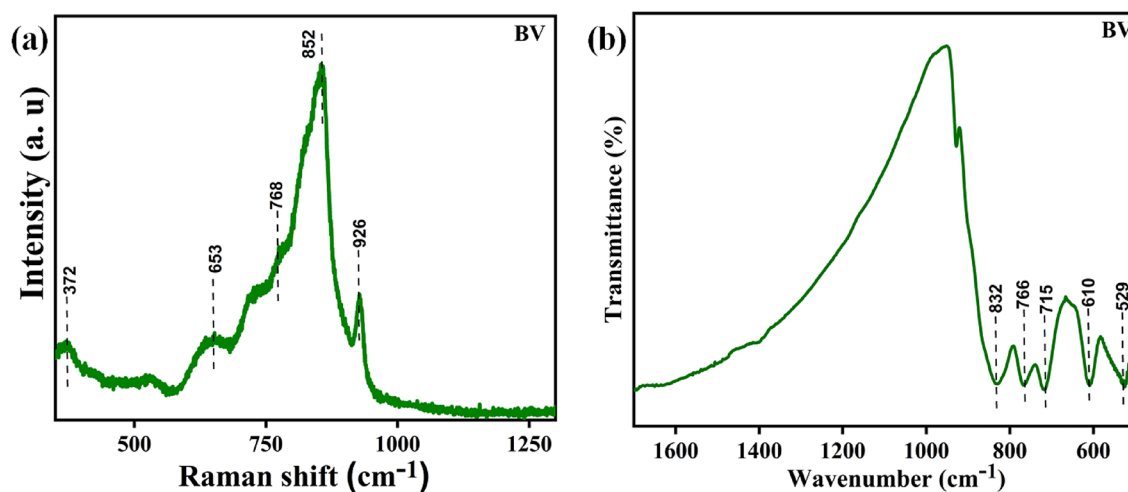


Figure 3. The BV sample's (a) Raman spectrum and (b) FTIR spectrum.

The SEM micrographs have been utilized to illustrate the sample's surface morphology as displayed in Fig. 4. Figure 4a–c provides clear proof of the presence of the BV sample's irregular-shaped grains. The not ball milled BiV sample's irregular shaped morphology is shown in Fig. 4d. We effectively decreased the particle size to the submicron range using the ball milling approach, as shown by the SEM micrographs. Figures 4c,d show the difference in particle size between the ball-milled $\text{Bi}_2\text{VO}_{5.5}$ (BV) sample and the not ball-milled $\text{Bi}_2\text{VO}_{5.5}$ (BiV) sample. For the BV sample, EDS elemental color mapping was carried out to achieve accurate phase identification. Figure 4e–f displays the chosen area of mapping and the presence of the O, V, and Bi elements.

To ascertain the elements' chemical states, the BV powdered sample underwent an XPS examination. The XPS spectra that correspond to the $\text{V}2p$, $\text{O}1s$, and $\text{Bi}4f$ scans are shown in Fig. 5a–c. Each of the asymmetric $\text{Bi}4f_{7/2}$ and $\text{Bi}4f_{5/2}$ components of the $\text{Bi}4f$ spectrum was initially separated into their respective Bi^{2+} and Bi^{3+} components. Two peaks, at 157.3 and 163.7 eV, are compatible with the Bi^{2+} oxidation state, while two more, at 158.8 and 164.1 eV, are consistent with the Bi^{3+} oxidation state^{57,58}. Each of the $\text{V}2p_{3/2}$ and $\text{V}2p_{1/2}$ components of the $\text{V}2p$ spectrum were initially separated into their respective V^{4+} and V^{5+} components. The V^{5+} oxidation state is shown by peaks at 516.4 and 524.2 eV, whereas the V^{4+} oxidation state is indicated by peaks at 517.3 and 523 eV⁵⁹. Asymmetric $\text{O}1s$ spectra were also first split into O_L and O_A sub-components. The O_L and O_A symbols represent oxygen vacancies and lattice oxygen (O^{2-} oxidation state), respectively⁵⁷. Intrinsic defects introduced during production and heat treatment lead to localized oxygen vacancies. Bi^{3+} and V^{5+} are converted to Bi^{2+} and V^{4+} , respectively, as a result of the bonded additional charge in the form of electron pairs surrounding the V and Bi atoms and in the vacant area. Consequently, we confirm the occurrence of Bi^{2+} and V^{4+} in addition to the previously documented Bi^{3+} and V^{5+} ⁶⁰.

Figure 6a depicts a time-dependent photocurrent study of a powdered BV sample, which was used to determine the charge carrier transportation behavior of the sample. BV achieves a low dark current density of

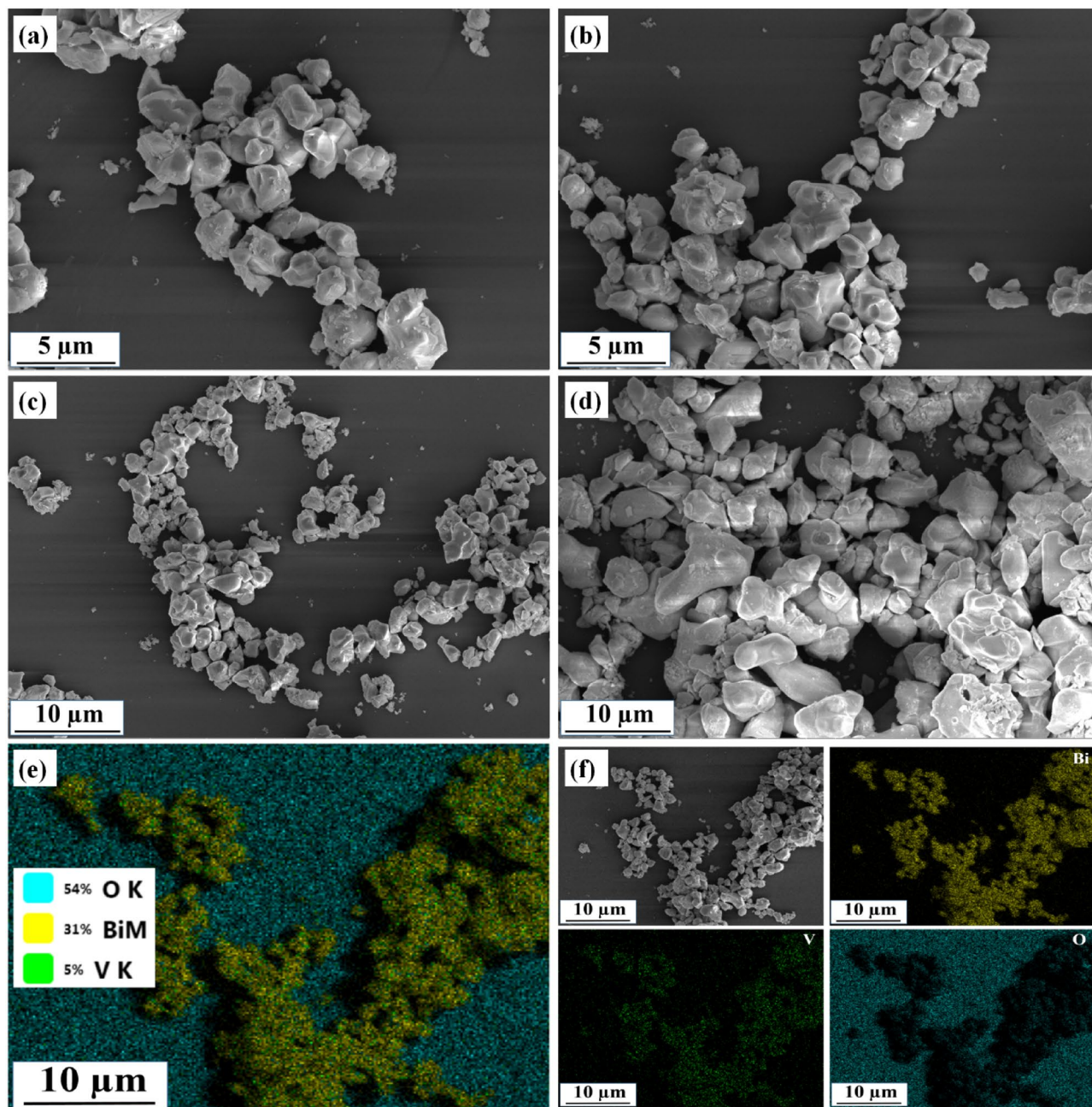


Figure 4. SEM photographs of (a–c) BV sample, (d) BiV sample, and (e–f) EDS elemental color mapping assessment of BV.

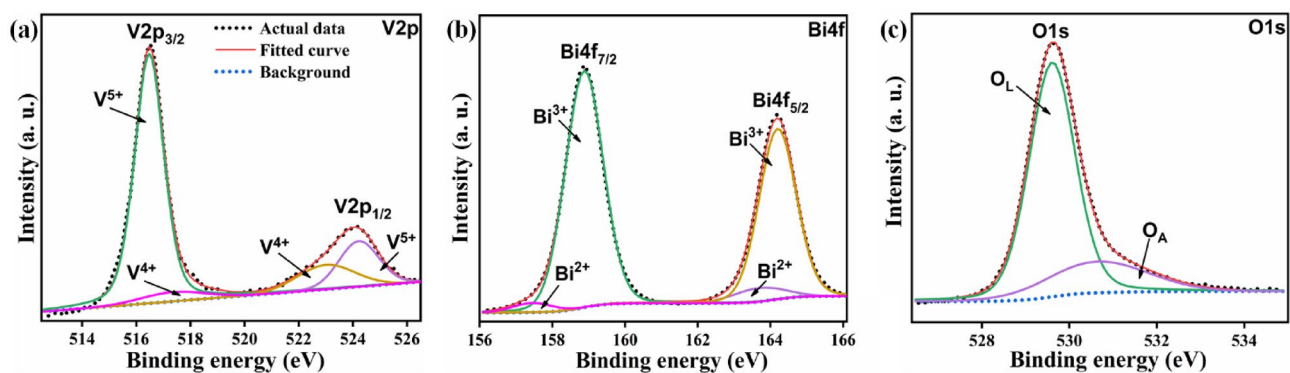


Figure 5. (a–c) The XPS spectra acquired for V2p, Bi4f, and O1s.

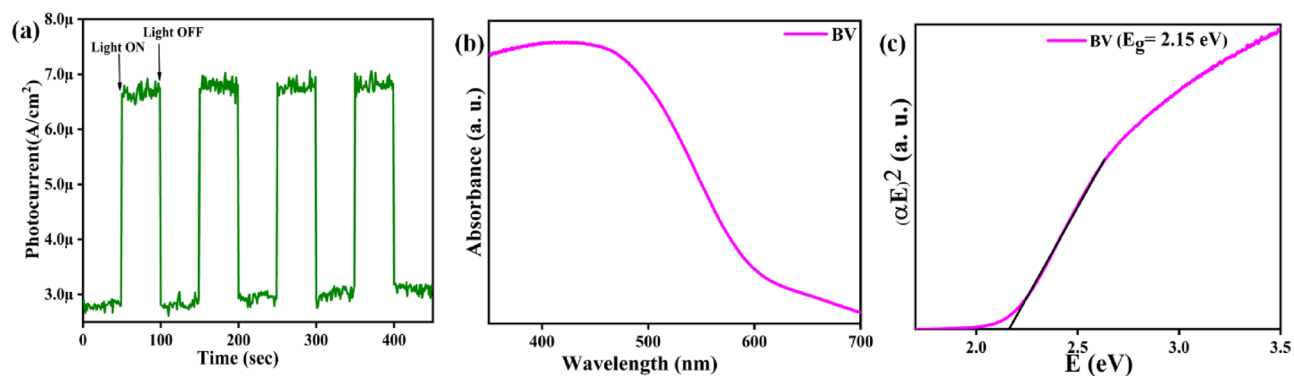


Figure 6. The BV sample's (a) Time-dependent photocurrent response (b) The absorbance spectrum (c) Tauc's plot.

($\sim 2.8 \mu\text{A}/\text{cm}^2$) before dye degradation, and it shows an increased photocurrent density of ($\sim 6.5 \mu\text{A}/\text{cm}^2$) when exposed to visible light. We were able to get a ratio of about 2.3 times between visible light and dark current as an outcome. Separation of the photogenerated charge carriers is facilitated by the formation of high photocurrent density. The BV sample's photocurrent response may be inverted, as shown by repeating the photocurrent density at each irradiation intensity^{61,62}.

Figure 6b depicts the diffuse reflectance spectrum (DRS) measured from the BV powdered sample. It displays the ball-milled BV sample's acquired optical absorption edge. The examined bandgap value of the BV sample is shown as 2.15 eV in Fig. 6c. Since the bandgap of BV is within the visible spectrum, the photocatalysis experiment may be carried out using visible light.

The photocatalysis experiment for the BV powder was evaluated by MB dye degradation, and the findings are shown in Fig. 7a. The dye's precise adsorption-desorption saturation was obtained before the start of the photocatalytic evaluation. Figure 7a shows that as the time duration of visible light irradiation was increased for the purpose of evaluating photocatalytic evaluation, the UV-visible absorption peak spectra of the MB dye dropped. The decreasing peak intensity with longer exposure time is proof that the polluting dye solution has become discolored. The $\frac{C}{C_0}$ versus time plots obtained for photocatalysis evaluation with BV, BiV, and without the usage of BV samples (control) are shown in Fig. 7b. Without a sample, photolysis caused the control dye to degrade by $\sim 12\%$ after 180 min when exposed to visible light. In 180-min visible light exposure, the MB degradation efficiencies of the BV and BiV samples were $\sim 29\%$ and $\sim 17\%$, respectively. In comparison to the control sample, the dye degradation efficiency of the BV and BiV samples improved by 17% and 5%, respectively. The variation in particle size between the BV and BiV samples, which has also been shown by SEM micrographs, is the cause of the discrepancy in the photocatalytic effectiveness reached by the two samples. We demonstrated that ball milling improved the catalytic performance by showing that BV's degradation efficiency was 12% higher than that of not ball mill synthesized BiV sample.

The BV powder piezocatalysis experiment was evaluated by monitoring the MB dye degradation, and the findings are displayed in Fig. 8a. As shown in Fig. 8a, the reduction in the MB dye's absorption peak spectrum with an increase in ultrasonication time served as proof that MB dye degradation occurred under ultrasonication. The decolorization of the pollutant solution is supported by the decreasing peak spectra with time. The $\frac{C}{C_0}$

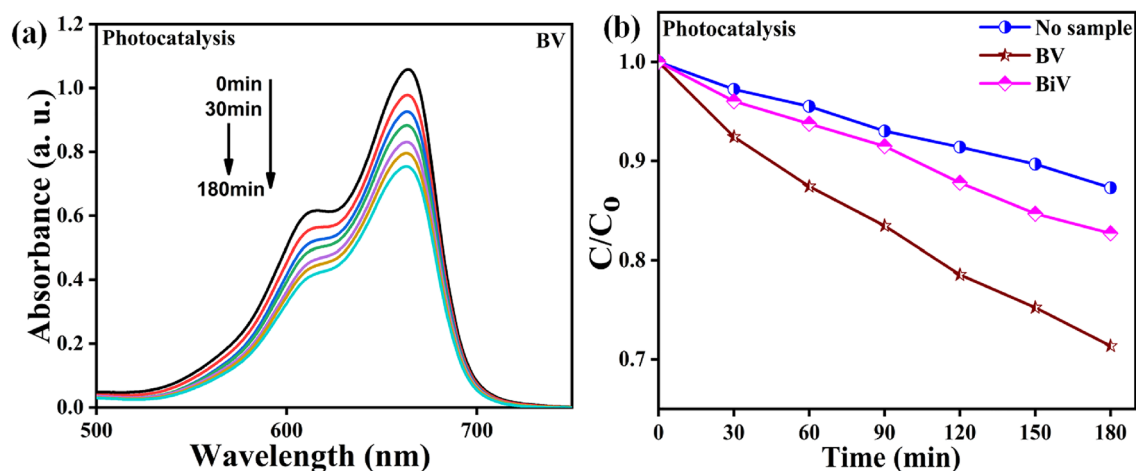


Figure 7. (a) Absorption spectra changes during photocatalytic testing with BV sample (b) $\frac{C}{C_0}$ versus time plots for photocatalytic testing with BV, BiV, and without samples.

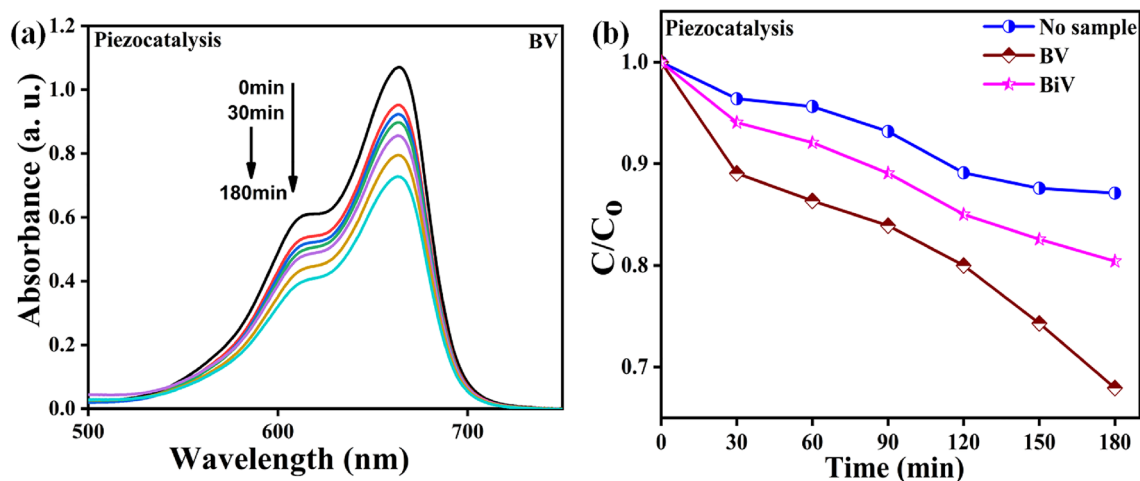


Figure 8. (a) Changes in absorption spectra during piezocatalytic testing with BV sample (b) $\frac{C}{C_0}$ versus time data obtained for piezocatalytic testing with BV, BiV, and without sample.

versus time data obtained for piezocatalysis evaluation with BV, BiV, and without the use of BV samples (control) are shown in Fig. 8b. Water bubbles that contain entrapped gases and water vapor form, grow and collapse as a result of the ultrasonication process⁶³. This activity generates a local hot zone where temperature increases up to 4000–5000 K^{63,64}. These localized hot zones promote the thermolytic breakdown of water, resulting in the generation of $\cdot\text{OH}$ radicals. These produced $\cdot\text{OH}$ radicals accelerate the degradation of MB dye. Sonolysis is the term used in literature to describe the entire phenomenon⁶⁵. To prevent the dye solution from heating up during ultrasonication, the water in the ultrasonicator was changed after every 15 min because it served as the medium for the process. In 180 min of ultrasonication, the control dye experienced 13% MB dye degradation in the absence of any sample. In the 180-min piezocatalysis experiment, the MB dye degradation efficiencies of the BV and BiV samples were $\sim 32\%$ and $\sim 20\%$, respectively. In comparison to the control sample, the dye degradation efficiency of the BV and BiV samples improved by 19% and 7%, respectively. The variation in particle size between the BV and BiV samples, which has also been shown by SEM micrographs, is the cause of the discrepancy in the piezocatalytic effectiveness reached by the two samples. We demonstrated that ball milling improved the catalytic performance by showing that BV's degradation efficiency was 12% higher than that of not ball mill synthesized BiV sample.

The BV powder piezo-photocatalytic experiment was evaluated by monitoring the MB dye degradation, and the findings are displayed in Fig. 9a. The dye's precise adsorption saturation was obtained before starting the piezo-photocatalysis evaluation. For evidence of MB dye degradation by piezo-photocatalysis, we tracked the time-dependent shift in the dye's absorption peak spectra, as shown in Fig. 9a. The decolorization of the pollutant solution is supported by the decreasing peak spectra with time. Water bubbles that contain entrapped gases and water vapor form, grow and collapse as a result of the ultrasonication process. This activity generates a local hot zone where temperature increases up to 4000–5000 K^{63,64}. These localized hot zones promote the thermolytic breakdown of water, resulting in the generation of $\cdot\text{OH}$ radicals. These produced $\cdot\text{OH}$ radicals accelerate the degradation of MB dye⁶⁶. To prevent the dye solution from heating up during the piezo-photocatalysis experiment, the water in the ultrasonicator was changed after every 15 min because it served as the medium for the process. The $\frac{C}{C_0}$ versus time chart obtained for piezo-photocatalysis evaluation of BV, BiV, and without the use of any sample (control) are shown in Fig. 9b. In a 180-min piezo-photocatalysis experiment, the control dye degrades by $\sim 19\%$ without the use of any samples. In 180 min of piezo-photocatalysis assessment, the MB degradation efficiencies of the BV and BiV samples were $\sim 63\%$ and $\sim 28\%$, respectively. In comparison to the control sample, the dye degradation efficiency of the BV and BiV samples improved by 44% and 9%, respectively. The variation in particle size between the BV and BiV samples, which has also been shown by SEM micrographs, is the cause of the discrepancy in the photocatalytic effectiveness reached by the two samples. We demonstrated that ball milling improved the catalytic performance by showing that BV's degradation efficiency was 35% higher than that of not ball mill synthesized BiV sample. The degradation efficiency of MB dye by piezo-photocatalysis, piezocatalysis, and photocatalysis on the BV sample is shown in Fig. 9c. During the evaluation of photocatalysis, piezocatalysis, and piezo-photocatalysis, BV powdered sample achieved the MB dye degradation efficiency of 29%, 32%, and 63%, respectively. It is evident that piezo-photocatalysis combination effects resulted in higher degradation efficiencies than individual piezocatalysis and individual photocatalysis studies were able to produce. The usage of a BV powdered sample demonstrated a 34% and 31% improvement in degradation performance during the piezo-photocatalysis as compared to the results of the individual photocatalysis and piezocatalysis experiment respectively. Because of the altered band structure brought on by the internal electric field, piezo-photocatalysis assessment results in greater utilization of the produced charge carriers^{67,68}. Additionally, current polarization effectively separates charge carriers, reducing the likelihood of charge recombination^{67,69}. Therefore, the piezo-photocatalysis dual effect may prove to be a useful strategy for increasing photocatalytic and piezocatalytic efficiency. During the investigation of the piezo-photocatalysis assessment, scavengers like isopropanol (IPA),

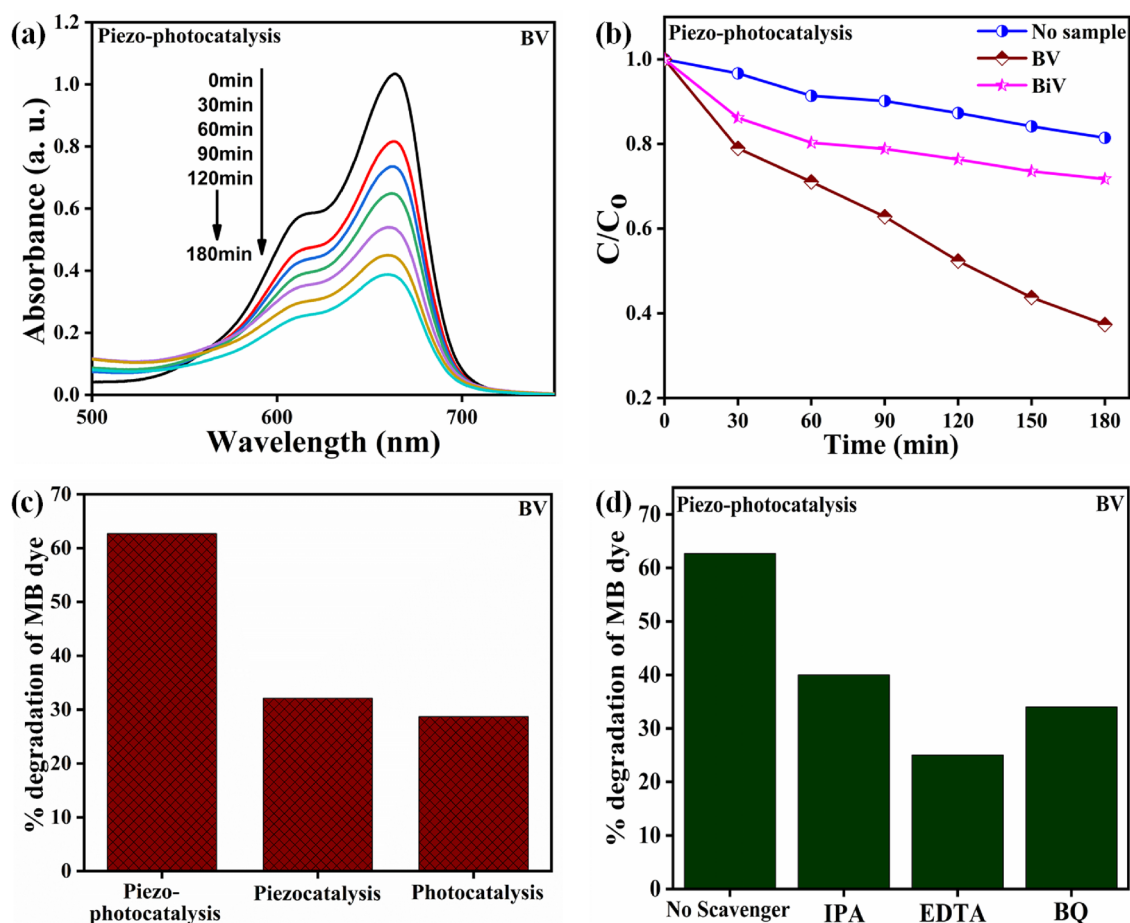


Figure 9. (a) Absorption spectra changes during photocatalytic testing with BV (b) $\frac{C}{C_0}$ versus time obtained for photocatalytic testing with BV, BiV, and without sample (c) evaluation of piezo-photocatalysis, piezocatalysis, and photocatalysis with BV (d) different scavengers effects examined using BV powders during piezo-photocatalytic analysis.

p-benzoquinone (p-BQ), and ethylenediaminetetraacetic acid (EDTA) were added separately to the dye solution to bind the active radical species such as the hydroxyl radical ($\cdot\text{OH}$), superoxide radical ($\cdot\text{O}_2^-$), and holes (h^+) respectively⁷⁰. Figure 9d shows how the piezo-photocatalysis assessment using the BV sample has been significantly impacted by the EDTA scavenger that preferably scavenges holes (h^+). Based on results from a scavenger assay, the principal active species in piezo-photocatalytic dye degradation are holes (h^+).

Figure 10a displays the $\frac{C}{C_0}$ versus time plots acquired during the piezo-photocatalysis evaluation utilizing BV powdered material at various dye concentrations (5, 10, and 15 mg/L). Figure 10b displays the $-\ln\left(\frac{C}{C_0}\right)$ versus time acquired during the piezo-photocatalysis assessment utilizing BV sample at different dye concentrations. The pseudo first-order kinetics described by Eq. 2 governs the piezo-photocatalytic degradation reaction in this instance^{71,72}.

$$\ln \frac{C}{C_0} = -kt \quad (2)$$

here “k” stands for the kinetic rate constant determined by the $\ln\left(\frac{C}{C_0}\right)$ versus time ‘t’ linear chart’s slope. The eminent k value of 0.00529 min^{-1} is attained here at a dye concentration of 5 mg/L and experiences a decrease in the value of k with enhancement in dye concentration. The obtained kinetic rate constants for varying dye concentrations of 5, 10, and 15 mg/L were 0.00529, 0.00218, and 0.00113 min^{-1} , respectively. Figure 10c presents the graph between the kinetic rate constant “k” and the various MB dye concentrations (5, 10, and 15 mg/L). The MB dye calibration curve is displayed in Fig. 10d. This curve was generated by measuring the distinctive peak absorbance intensity of MB dye at varied concentrations (0, 5, 10, 15, and 20 mg/L). Figure 10d demonstrates a linear relationship between absorbance and concentration. With the use of this curve, the absorbance intensity value of the dye solution used in the catalysis experiment may be determined. Some detailed study can be found in supplementary data S1.

To investigate the sustainability, reusability, and appropriateness of the cleansed wastewater following the piezo-photocatalysis assessment, a simplified germination index (GI) test had been conducted, wherein seed

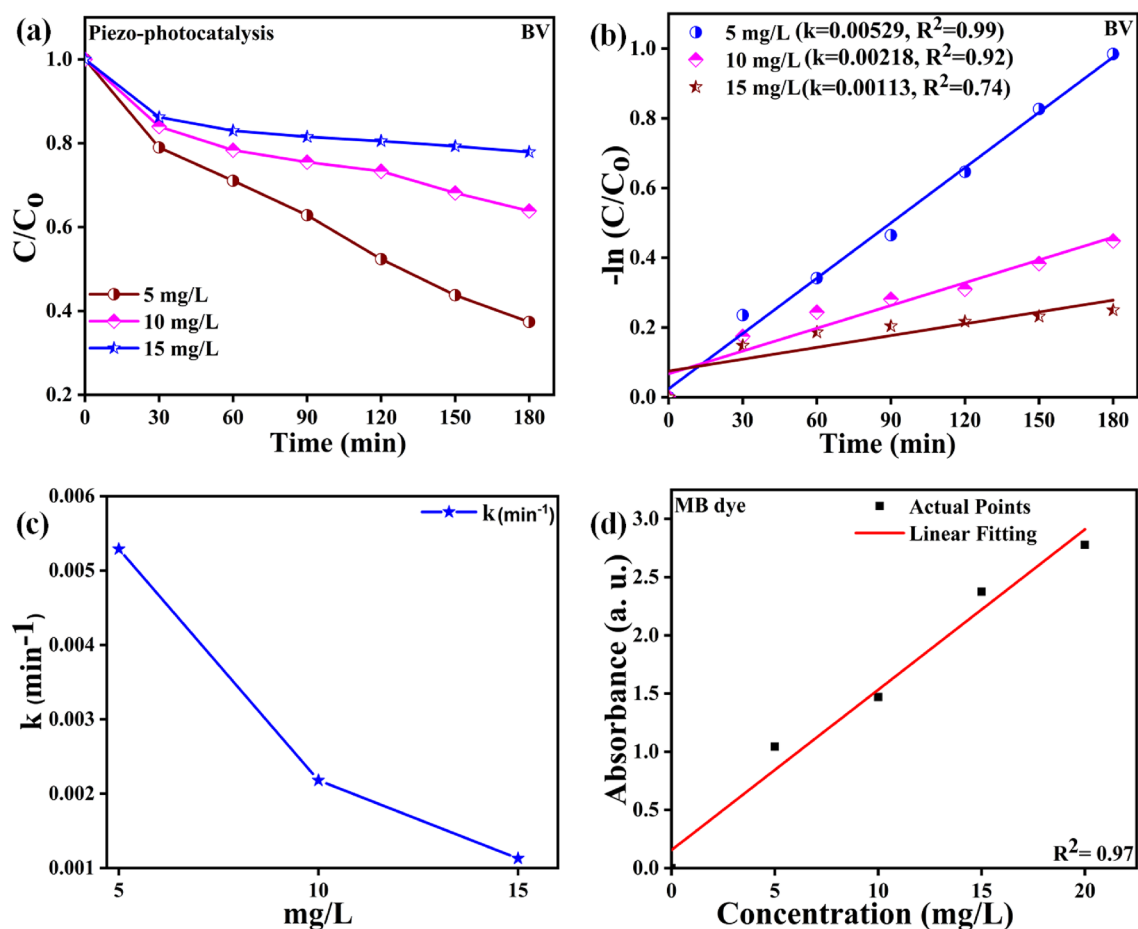


Figure 10. (a) $\frac{C}{C_0}$ versus time chart for piezo-photocatalytic evaluation at varying dye concentration (b) $-\ln\left(\frac{C}{C_0}\right)$ versus time chart for piezo-photocatalytic evaluation at varying dye concentrations (c) plot across the kinetic rate constant ' k ' versus concentration of MB dye (mg/L) and (d) calibration curve of MB dye.

germination along with their complete growth had been assessed. *Vigna radiata* seeds were obtained from Dr. Rajendra Prasad Central Agricultural University, Bihar. All the experiments were performed following relevant guidelines. Each of the three vials contained 10 *Vigna radiata* seeds, which received daily 0.5 ml each of untreated, treated, and distilled water sprinkling. The evaluation of the test was completed over seven days in India's IIT Mandi, wherein the average outside temperature noted was 30 °C. Figure 11a–c shows seed growth in three different scenarios: dye water before being subjected to piezo-photocatalysis, dye water after piezo-photocatalysis, and distilled water. It was shown that the majority of hurdles towards the growth of seed were associated with untreated 5 mg/L dye, whereas seed growth under the influence of the treated water is non-toxic⁷³. However, edible plants require further protection, and any negative effects must be effectively managed. As an alternative to watering edible plants, we propose using this treated wastewater for playground irrigation⁷⁴. The need for water will thereby be partially reduced. Results for phytotoxicity are displayed in Fig. 11d. Emino et al. have proposed three classes for substances based on GI values: strong phytotoxicity ($GI < 50\%$), moderate phytotoxicity ($50\% < GI < 80\%$), and no phytotoxicity ($GI > 80\%$)^{72,75}. According to the findings, whereas untreated dye has a high degree of toxicity, treated water has a moderate level of toxicity^{72,75}. Here, a piezo-photocatalysis evaluation of the treated water utilized for the germination of the seed had only achieved 63% of dye degradation efficiency. By increasing the catalytic load, lengthening the catalytic time span, and lowering dye concentration, it is also possible to achieve 100% dye purification efficiency, which would further increase the germination index^{21,76}.

A description of the mechanism incurred by BV while the degradation pathway of MB dye under the photocatalysis, piezocatalysis, and piezo-photocatalysis studies is shown in Fig. 12a–c. The mechanism of photocatalysis is shown in Fig. 12a, wherein the synthesized BV phase forms electron–hole pairs in response to light stimulation. Superoxide radicals (O_2^-) are produced when electrons react with adsorbed oxygen, whereas hydroxyl radicals (OH^\cdot) are produced when holes oxidize the adsorbed water. Reactive oxidizing species (ROS) include species like (O_2^-) and (OH^\cdot), which degrade MB dye into innocuous end products. As a result, photocatalytic activity occurs^{4,44}.

The piezocatalysis mechanism is presented in Fig. 12b. The cavitation process creates local hot spots, which exert forces on the BV surface to cause local strain⁶⁶. The strain induced by ultrasonication leads to the formation of polarization charges (an internal electric field) on the surface of BV. Internal electric field influence causes the

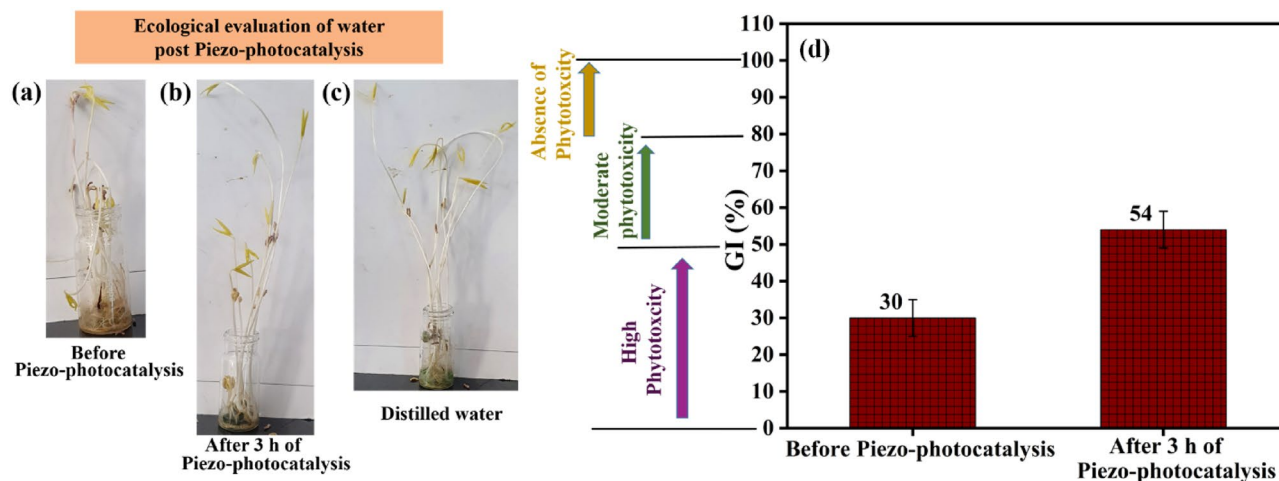


Figure 11. Effect of MB dye on the development of *Vigna radiata* seeds over the course of 7 days. The evaluation was conducted using (a) 5 mg/L MB dye (b) treated wastewater (c) distilled water (d) Analysis of the germination index on 2 samples taken after 0 and 3 h after the piezo-photocatalysis experiment.

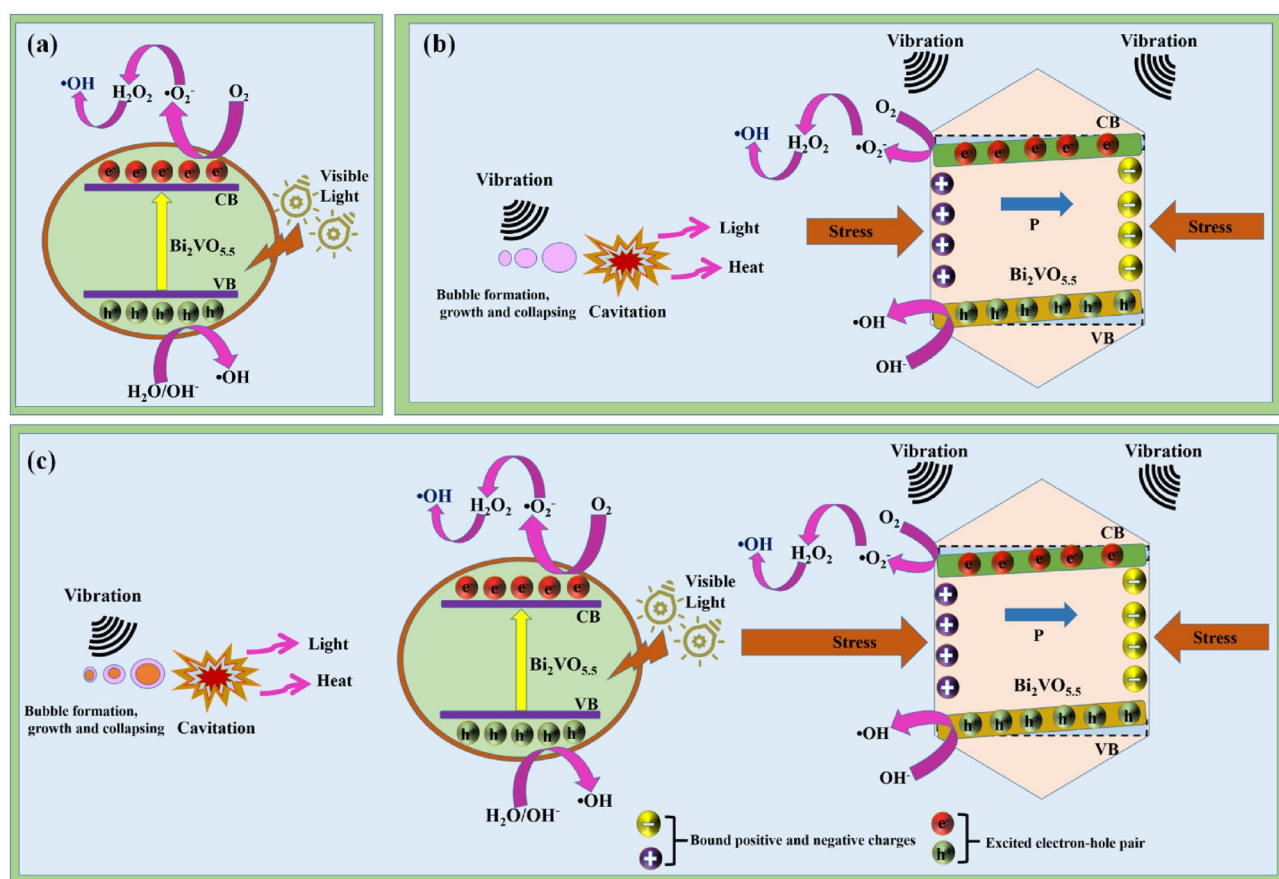


Figure 12. Mechanism incurred by BV during the evaluation of (a) photocatalysis (b) piezocatalysis (c) piezo-photocatalysis.

free electron-hole pairs to shift to the opposite polarity, aiding in the dissociation of e^- - h^+ pairs^{77,78}. As a result, the BV surface has increased free charge accumulation since the probability of charge carrier recombination is suppressed^{69,79}. Although there is still disagreement over the potential charge carriers source during the ultrasonication process, it is thought that sonoluminescence (during ultrasonication, light is produced at a wavelength of 375 nm) and heat rise due to hot spot creation may be the source^{80,81}. Ultrasonication with phenomena like polarization may have a synergistic effect. Additionally, polarization-induced band bending aids in the transport of e^- and h^+ to the BV surface. These are not photogenerated e^- and h^+ because the piezocatalysis occurs in the

dark. Superoxide radicals ($O_2^{\cdot-}$) are produced when electrons interact with adsorbed oxygen, whereas hydroxyl radicals (OH^{\cdot}) are produced when holes oxidize the adsorbed water. These ROS also contribute to the formation of innocuous end products as MB dye degrades^{44,63,64}. Consequently, piezocatalytic activity occurs.

The piezo-photocatalysis mechanism is presented in Fig. 12c. The valence band (VB) electrons are stimulated by visible light to move into the conduction band (CB), while the VB holes are left behind, creating electron–hole pairs in the BV phase⁸². Although there is still disagreement over the charge carriers source during the ultrasonication process, it is thought that sonoluminescence (during ultrasonication, light is produced at a wavelength of 375 nm) and heat rise due to hot spot creation may be the source^{80,81}. Ultrasonication with phenomena like polarization may have a synergistic effect. In piezo-photocatalysis, thermally excited holes and electrons predominate over photo-excited ones, which are in minor concentration. As a result, the addition of ultrasonication and visible light improves the concentration of free charges on the surface of the semiconductor catalysts⁸³. The stress created during ultrasonication induces polarization charges on the BV surface. Local hot spots are formed as a consequence of the cavitation process, and these hot spots act on the BV surface to produce local strain^{63,64}. A positive polarization charge is created at the surface by a ferroelectric domain whose orientation is from the bulk to the surface, whereas a negative charge is produced by a domain whose orientation is from the surface to the bulk. By doing so, an electric field within the BV can be created. Positive and negative polarization charges on the BV will attract photogenerated electrons and holes, accordingly⁸⁴. The energy band is shifted downward at the positive polarization charge side and shifted upward at the negative polarization charge side, as shown in Fig. 12c. As a result of band bending brought on by polarization, photo-excited electrons are further moved to a lower energy level whereas the photogenerated holes in the VB are moved to an elevated energy level⁸⁵. The dominant polarization prevents recombination between electrons and holes by increasing the space between the charge carriers, which sends electrons and holes in opposite directions⁷⁸. As a result, the BV surface will have more electrons and holes available, which will increase the generation of radicals. It is energetically more desirable for both holes and electrons to take part in redox processes. Thus, the catalytic redox reaction is improved, speeding up the efficiency of dye degradation. Electrons reacting with adsorbed oxygen create superoxide radicals ($O_2^{\cdot-}$), while hydroxyl radicals (OH^{\cdot}) are produced when holes oxidize the adsorbed water. These ROS also contribute to the innocuous end products formed as MB dye degrades^{44,63}. The enhanced catalytic degradation can be traced back to the link between polarization potential and photoexcitation effects, which facilitates photogenerated electron–hole pairs separation and effectively suppresses carrier recombination. Consequently, piezo-photocatalytic activity occurs.

Conclusions

The ball-milled $Bi_2VO_{5.5}$ powder was investigated to achieve improved piezo-photocatalytic efficiency after it was produced through mechanochemical ball milling synthesis at 650 °C for 5 h. By successfully segregating charge carriers, the catalyst efficiently utilized the synergetic impact of visible light irradiation along with ultrasonic vibration for enhanced dye degradation. The effectiveness of dye degradation achieved through piezo-photocatalysis, piezocatalysis, and photocatalysis was examined, along with the process of degradation. The piezo-photocatalysis assessment obtains a dye degradation efficiency of ~63% using a $Bi_2VO_{5.5}$ powdered sample. The dye disintegration follows a pseudo-first-order kinetic and reaches a maximum k value of 0.0053 min^{-1} . Reduced particle size attained through the ball milling synthesis of the $Bi_2VO_{5.5}$ sample along with synergetic piezo-photocatalysis assessment has contributed to attaining higher dye degradation efficiency.

Data availability

This manuscript includes all relevant data.

Received: 2 February 2023; Accepted: 17 April 2023

Published online: 20 May 2023

References

- Xie, W. *et al.* Photocatalytic performance of $Bi_2VO_{5.5}/Bi_2O_3$ laminated composite films under simulated sunlight irradiation. *Solid State Sci.* **94**, 1–7 (2019).
- Lv, T. *et al.* Facile synthesis of $CdS/Bi_4V_2O_{11}$ photocatalysts with enhanced visible-light photocatalytic activity for degradation of organic pollutants in water. *Dalt. Trans.* **46**, 12675–12682 (2017).
- He, Y. *et al.* Efficient degradation of RhB over $GdVO_4/g-C_3N_4$ composites under visible-light irradiation. *Chem. Eng. J.* **215**, 721–730 (2013).
- Zhao, Y., Liu, X., Gu, S. & Liu, J. Enhanced photocatalytic performance of rhodamine B and enrofloxacin by Pt loaded $Bi_4V_2O_{11}$: boosted separation of charge carriers, additional superoxide radical production, and the photocatalytic mechanism. *RSC Adv.* **11**, 9746–9755 (2021).
- Nasuha, N., Hameed, B. H. & Din, A. T. M. Rejected tea as a potential low-cost adsorbent for the removal of methylene blue. *J. Hazard. Mater.* **175**, 126–132 (2010).
- Martin, M. J., Artola, A., Balaguer, M. D. & Rigola, M. Activated carbons developed from surplus sewage sludge for the removal of dyes from dilute aqueous solutions. *Chem. Eng. J.* **94**, 231–239 (2003).
- Ri, C.-N. *et al.* The synthesis of a $Bi_2MoO_6/Bi_4V_2O_{11}$ heterojunction photocatalyst with enhanced visible-light-driven photocatalytic activity. *RSC Adv.* **8**, 5433–5440 (2018).
- Vadivel, S. *et al.* Facile synthesis of novel $CaFe_2O_4/g-C_3N_4$ nanocomposites for degradation of methylene blue under visible-light irradiation. *J. Colloid Interface Sci.* **480**, 126–136 (2016).
- Kumar, S. & Sahare, P. D. Photocatalytic activity of bismuth vanadate for the degradation of organic compounds. *NANO* **8**, 1350007 (2013).
- Tantak, N. P. & Chaudhari, S. Degradation of azo dyes by sequential Fenton's oxidation and aerobic biological treatment. *J. Hazard. Mater.* **136**, 698–705 (2006).

11. Laowansiri, S., Vinitnantharat, S., Chairprasert, P. & Ha, S. R. Anaerobic degradation kinetics of reactive dye with different carbon sources. *J. Environ. Biol.* **29**, 309 (2008).
12. Chandrasekaran, S. *et al.* Spinel photocatalysts for environmental remediation, hydrogen generation, CO₂ reduction and photo-electrochemical water splitting. *J. Mater. Chem. A* **6**, 11078–11104 (2018).
13. Liu, J. *et al.* Enhanced electron separation on in-plane benzene-ring doped g-C₃N₄ nanosheets for visible light photocatalytic hydrogen evolution. *Appl. Catal. B Environ.* **244**, 459–464 (2019).
14. An, X., Hu, C., Liu, H. & Qu, J. Oxygen vacancy mediated construction of anatase/brookite heterophase junctions for high-efficiency photocatalytic hydrogen evolution. *J. Mater. Chem. A* **5**, 24989–24994 (2017).
15. Lv, C. *et al.* Realizing nanosized interfacial contact via constructing BiVO₄/Bi₄V₂O₁₁ element-copied heterojunction nanofibres for superior photocatalytic properties. *Appl. Catal. B Environ.* **179**, 54–60 (2015).
16. Di Paola, A., García-López, E., Marci, G. & Palmisano, L. A survey of photocatalytic materials for environmental remediation. *J. Hazard. Mater.* **211**, 3–29 (2012).
17. Tang, J., Zou, Z. & Ye, J. Efficient photocatalytic decomposition of organic contaminants over CaBi₂O₄ under visible-light irradiation. *Angew. Chemie* **116**, 4563–4566 (2004).
18. Chen, X., Liu, L., Yu, P. Y. & Mao, S. S. Increasing solar absorption for photocatalysis with black hydrogenated titanium dioxide nanocrystals. *Science (80-)* **331**, 746–750 (2011).
19. Chen, H., Nanayakkara, C. E. & Grassian, V. H. Titanium dioxide photocatalysis in atmospheric chemistry. *Chem. Rev.* **112**, 5919–5948 (2012).
20. Li, Z. *et al.* Novel application of Ag/PbBiO₂I nanocomposite in piezocatalytic degradation of rhodamine B via harvesting ultrasonic vibration energy. *Ultrason. Sonochem.* **78**, 105729 (2021).
21. Tu, S. *et al.* Piezocatalysis and piezo-photocatalysis: catalysts classification and modification strategy, reaction mechanism, and practical application. *Adv. Funct. Mater.* **30**, 1–31 (2020).
22. Cao, S., Zhou, P. & Yu, J. Recent advances in visible light Bi-based photocatalysts. *Chinese J. Catal.* **35**, 989–1007 (2014).
23. Kako, T. & Ye, J. Photocatalytic decomposition of acetaldehyde over rubidium bismuth niobates under visible light irradiation. *Mater. Trans.* **46**, 2694–2698 (2005).
24. Kumar, V. R., Prasad, V. S., Warier, P. R. S. & Koshy, J. Synthesis, characterization and photocatalytic activities of Ba₂YbZrO_{5.5} nanoparticles under solar irradiation. *NANO* **6**, 279–286 (2011).
25. Ramachandran, R. *et al.* Photocatalytic properties of KBiO₃ and LiBiO₃ with tunnel structures. *J. Chem. Sci.* **123**, 517–524 (2011).
26. Xie, W., Hu, W., Zou, L. & Bao, D. Enhanced photocatalytic activity and dielectric property of c-axis oriented Bi₂VO_{5.5} thin film by Gd³⁺ doping. *Ceram. Int.* **41**, S265–S273 (2015).
27. Guo, W., Fan, K., Zhang, J. & Xu, C. 2D/2D Z-scheme Bi₂WO₆/Porous-g-C₃N₄ with synergy of adsorption and visible-light-driven photodegradation. *Appl. Surf. Sci.* **447**, 125–134 (2018).
28. Naqvi, F. K., Faraz, M., Beg, S. & Khare, N. Synthesis and phase transformation studies of dysprosium-doped Bi₄V₂O₁₁ nanoparticles and their application in visible light photocatalytic degradation of tetracycline drug. *ACS Omega* **3**, 11300–11306 (2018).
29. Gao, X.-M., Fu, F. & Li, W.-H. Photocatalytic degradation of phenol over Cu loading BiVO₄ metal composite oxides under visible light irradiation. *Phys. B Condens. Matter* **412**, 26–31 (2013).
30. Kumari, N., Krupanidhi, S. B. & Varma, K. B. R. Dielectric, impedance and ferroelectric characteristics of c-oriented bismuth vanadate films grown by pulsed laser deposition. *Mater. Sci. Eng. B* **138**, 22–30 (2007).
31. Kumari, N., Krupanidhi, S. B. & Varma, K. B. R. Structural and electrical studies on Bi₂VO_{5.5}/Bi₄Ti₃O₁₂ multilayer thin films. *J. Mater. Sci. Mater. Electron.* **22**, 639–648 (2011).
32. de yDompablo, M. E. A., Garcia-Alvarado, F. & Moran, E. Bi₄V₂O₁₁ and related compounds as positive electrode materials for lithium rechargeable batteries. *Solid State Ion.* **91**, 273–278 (1996).
33. Pookmanee, P., Intaphong, P., Phanmalee, J., Kangwansupamonkon, W. & Phanichphant, S. Characterization of bismuth vanadate nanopowder prepared by microwave method. in *Materials Science Forum* vol. 872, pp 253–257 (Trans Tech Publ, 2016).
34. Kumar, M. *et al.* Piezo-photocatalytic activity of Bi₂VO_{5.5} for methylene blue dye degradation. *J. Mater. Res. Technol* **21**, 1998–2012 (2022).
35. Pell, J. W., Ying, J. Y. & zur Loye, H.-C. Sol-gel synthesis of α-Bi₂VO_{5.5} using a soluble bismuth precursor. *Mater. Lett.* **25**, 157–160 (1995).
36. Vaidhyanathan, B., Ganguli, M. & Rao, K. J. Fast solid state synthesis of metal vanadates and chalcogenides using microwave irradiation. *Mater. Res. Bull.* **30**, 1173–1177 (1995).
37. Joseph, M., Lee, H. Y., Tabata, H. & Kawai, T. Ferroelectric behavior of epitaxial Bi₂VO_{5.5} thin films on Si (100) formed by pulsed-laser deposition. *J. Appl. Phys.* **88**, 1193–1195 (2000).
38. Kumari, N., Parui, J., Varma, K. B. R. & Krupanidhi, S. B. C-V studies on metal-ferroelectric bismuth vanadate (Bi₂VO_{5.5})-semiconductor structure. *Solid State Commun.* **137**, 566–569 (2006).
39. Zhu, Q. *et al.* Efficient full spectrum responsive photocatalytic NO conversion at Bi₂Ti₂O₇: Co-effect of plasmonic bi and oxygen vacancy. *Appl. Catal. B Environ.* **319**, 121888 (2022).
40. Kumari, N., Krupanidhi, S. B. & Varma, K. B. R. Structural, ferroelectric and optical properties of Bi₂VO_{5.5} thin films deposited on platinized silicon (100) Pt/TiO₂/SiO₂/Si substrates. *Appl. Phys. A* **91**, 693–699 (2008).
41. Paramesh, G., Kumari, N., Krupanidhi, S. B. & Varma, K. B. R. Large nonlinear refraction and two photon absorption in ferroelectric Bi₂VO_{5.5} thin films. *Opt. Mater. (Amst)* **34**, 1822–1825 (2012).
42. Wang, J. M. *et al.* Synthesis of BiVO₄/Bi₂VO_{5.5} Heterogeneous nanostructures with enhanced visible light photocatalytic activity. in *Materials Science Forum* vol. 847, pp. 211–217 (Trans Tech Publ, 2016).
43. Castro, A., Millán, P., Ricote, J. & Pardo, L. Room temperature stabilisation of γ-Bi₂VO_{5.5} and synthesis of the new fluorite phase f-Bi₂VO₅ by a mechanochemical activation method. *J. Mater. Chem.* **10**, 767–771 (2000).
44. Kumar, M., Vaish, R. & ben Ahmed, S. Piezo-photocatalytic activity of mechanochemically synthesized BiVO₄ for dye cleaning. *J. Am. Ceram. Soc.* **105**(3), 2309–2322 (2022).
45. Luo, Q., Zhang, L., Chen, X., Tan, O. K. & Leong, K. C. Mechanochemically synthesized m-BiVO₄ nanoparticles for visible light photocatalysis. *RSC Adv.* **6**, 15796–15802 (2016).
46. Guan, M.-L., Ma, D.-K., Hu, S.-W., Chen, Y.-J. & Huang, S.-M. From hollow olive-shaped BiVO₄ to n-p core-shell BiVO₄@Bi₂O₃ microspheres: Controlled synthesis and enhanced visible-light-responsive photocatalytic properties. *Inorg. Chem.* **50**, 800–805 (2011).
47. Phanmalee, J., Intaphong, P., Kangwansupamonkon, W., Phanichphant, S. & Pookmanee, P. The Photocatalytic degradation of methylene blue using bismuth vanadate (Bi₂VO_{5.5}) Powder. in *Key Engineering Materials* vol. 751 707–712 (Trans Tech Publ, 2017).
48. Xie, W., Qin, N., Li, B. & Bao, D. Enhanced visible-light catalytic activity of Au nanoparticles loaded c-axis oriented Bi₂VO_{5.5} porous thin films. *Ceram. Int.* **41**, 8433–8443 (2015).
49. Ebrahimi-Purkani, A. & Kashani-Bozorg, S. F. Nanocrystalline Mg₂Ni-based powders produced by high-energy ball milling and subsequent annealing. *J. Alloys Compd.* **456**, 211–215 (2008).
50. Zhang, D. *et al.* Facile in situ chemical transformation synthesis, boosted charge separation, and increased photocatalytic activity of BiPO₄/BiOCl pn heterojunction photocatalysts under simulated sunlight irradiation. *J. Phys. Chem. Solids* **147**, 109630 (2020).
51. Nabi, G., Malik, N. & Raza, W. Degradation effect of temperature variation and dye loading g-C₃N₄ towards organic dyes. *Inorg. Chem. Commun.* **119**, 108050 (2020).

52. Patwe, S. J. *et al.* Probing the local structure and phase transitions of $\text{Bi}_4\text{V}_2\text{O}_{11}$ -based fast ionic conductors by combined raman and XRD studies. *J. Am. Ceram. Soc.* **96**, 3448–3456 (2013).
53. Dimitrov, V., Dimitriev, Y. & Montenero, A. IR spectra and structure of V_2O_5 , GeO_2 , Bi_2O_3 glasses. *J. Non. Cryst. Solids* **180**, 51–57 (1994).
54. Abd El-Moneim, A. DTA and IR absorption spectra of vanadium tellurite glasses. *Mater. Chem. Phys.* **73**, 318–322 (2002).
55. Tripathy, D., Saikia, A., Tado, G. T. & Pandey, A. Dielectric study of Ti-doped $\text{Bi}_2\text{VO}_{5.5}$ solid electrolyte. *Indian J. Phys.* **93**, 845–859 (2019).
56. Tripathy, D., Saikia, A. & Pandey, A. Effect of simultaneous Ti and Nb doping on structure and ionic conductivity of $\text{Bi}_2\text{V}_{1-x}\text{Ti}_x/2\text{Nb}_{x/2}\text{O}_{5.5-\delta}$ ($0.1 \leq x \leq 0.25$) ceramics. *Ionics* **25**, 2221–2230 (2019).
57. Lv, C. *et al.* Oxygen-induced Bi^{3+} -self-doped $\text{Bi}_4\text{V}_2\text{O}_{11}$ with ap–n homojunction toward promoting the photocatalytic performance. *ACS Appl. Mater. Interfaces* **9**, 23748–23755 (2017).
58. Liu, Z., Niu, J., Feng, P., Sui, Y. & Zhu, Y. One-pot synthesis of $\text{Bi}_{24}\text{O}_{31}\text{Br}_{10}\text{Bi}_4\text{V}_2\text{O}_{11}$ heterostructures and their photocatalytic properties. *RSC Adv.* **4**, 43399–43405 (2014).
59. Anwar, K., Naqvi, F. K. & Beg, S. Synthesis of tetragonally stabilized lanthanum doped bismuth vanadium oxide nanoparticles and its enhanced visible light induced photocatalytic performance. *Phase Trans.* **95**, 64–79 (2022).
60. Daelman, N. *et al.* Quasi-degenerate states and their dynamics in oxygen deficient reducible metal oxides. *J. Chem. Phys.* **152**, 50901 (2020).
61. Fan, C.-M. *et al.* Synproportionation reaction for the fabrication of Sn^{2+} self-doped SnO_{2-x} nanocrystals with tunable band structure and highly efficient visible light photocatalytic activity. *J. Phys. Chem. C* **117**, 24157–24166 (2013).
62. Xia, J. *et al.* Highly monodisperse $\text{Cu}_3\text{Mo}_2\text{O}_9$ micropomons with excellent performance in photocatalysis, photocurrent response and lithium storage. *RSC Adv.* **5**, 12015–12024 (2015).
63. Kumar, M., Singh, G. & Vaish, R. Reduced graphene oxide/bismuth vanadate composite as an efficient piezocatalyst for degradation of organic dye. *Mater. Adv.* **2**(12), 4093–4101 (2021).
64. Singh, K. P., Singh, G. & Vaish, R. Utilizing the localized surface piezoelectricity of centrosymmetric $\text{Sr}_{1-x}\text{FexTiO}_3$ ($x \leq 0.2$) ceramics for piezocatalytic dye degradation. *J. Eur. Ceram. Soc.* **41**, 326–334 (2021).
65. Ghows, N. & Entezari, M. H. Kinetic investigation on sono-degradation of Reactive Black 5 with core–shell nanocrystal. *Ultrason. Sonochem.* **20**, 386–394 (2013).
66. Tezcanli-Güyer, G. & Ince, N. H. Individual and combined effects of ultrasound, ozone and UV irradiation: A case study with textile dyes. *Ultrasonics* **42**, 603–609 (2004).
67. Morris, M. R., Pendlebury, S. R., Hong, J., Dunn, S. & Durrant, J. R. Effect of internal electric fields on charge carrier dynamics in a ferroelectric material for solar energy conversion. *Adv. Mater.* **28**, 7123–7128 (2016).
68. Yang, W. *et al.* Ferroelectric polarization-enhanced photoelectrochemical water splitting in TiO_2 – BaTiO_3 core–shell nanowire photoanodes. *Nano Lett.* **15**, 7574–7580 (2015).
69. Yang, Q., Wang, W., Xu, S. & Wang, Z. L. Enhancing light emission of ZnO microwire-based diodes by piezo-phototronic effect. *Nano Lett.* **11**, 4012–4017 (2011).
70. Singh, G., Kumar, M. & Vaish, R. Promising multicatalytic and adsorption capabilities in $\text{V}_2\text{O}_5/\text{BiVO}_4$ composite pellets for water-cleaning application. *Surf. Interfaces* **23**, 100924 (2021).
71. Singh, R. P. *et al.* Synthesis of $\text{Ag}_2\text{V}_4\text{O}_{11}$ nanoflakes mediated photoactivation of peroxymonosulfate ion for enhanced dye degradation and intrinsic bactericidal activity. *Mater. Sci. Semicond. Process.* **143**, 106526 (2022).
72. Kumar, M. *et al.* Sonophotocatalytic dye degradation using rGO– BiVO_4 composites. *Glob. Chall.* **6**(6), 2100132 (2022).
73. Priac, A., Badot, P.-M. & Crini, G. Treated wastewater phytotoxicity assessment using *Lactuca sativa*: Focus on germination and root elongation test parameters. *C. R. Biol.* **340**, 188–194 (2017).
74. Singh, A., Bhati, A., Khare, P., Tripathi, K. M. & Sonkar, S. K. Soluble graphene nanosheets for the sunlight-induced photodegradation of the mixture of dyes and its environmental assessment. *Sci. Rep.* **9**, 1–12 (2019).
75. Emimo, E. R. & Warman, P. R. Biological assay for compost quality. *Compost Sci. Util.* **12**, 342–348 (2004).
76. Kumar, A. & Pandey, G. A review on the factors affecting the photocatalytic degradation of hazardous materials. *Mater. Sci. Eng. Int. J* **1**, 1–10 (2017).
77. Zhao, Z. *et al.* Exclusive enhancement of catalytic activity in $\text{Bi}_{0.5}\text{Na}_{0.5}\text{TiO}_3$ nanostructures: new insights into the design of efficient piezocatalysts and piezo-photocatalysts. *J. Mater. Chem. A* **8**, 16238–16245 (2020).
78. Zhu, Q. *et al.* Polarization-enhanced photocatalytic activity in non-centrosymmetric materials based photocatalysis: A review. *Chem. Eng. J.* **426**, 131681 (2021).
79. Feng, W. *et al.* Hydrogenated TiO_2/ZnO heterojunction nanorod arrays with enhanced performance for photoelectrochemical water splitting. *Int. J. Hydrog. Energy* **42**, 3938–3946 (2017).
80. Zhu, L., Meng, Z.-D., Park, C.-Y., Ghosh, T. & Oh, W.-C. Characterization and relative sonocatalytic efficiencies of a new MWCNT and CdS modified TiO_2 catalysts and their application in the sonocatalytic degradation of rhodamine B. *Ultrason. Sonochem.* **20**, 478–484 (2013).
81. Lei, H. *et al.* Synergetic photocatalysis/piezocatalysis of bismuth oxybromide for degradation of organic pollutants. *J. Alloys Compd.* **809**, 151840 (2019).
82. Ganeshbabu, M. *et al.* Synthesis and characterization of BiVO_4 nanoparticles for environmental applications. *RSC Adv.* **10**, 18315–18322 (2020).
83. Lin, E. *et al.* Enhanced piezocatalytic, photocatalytic and piezo-/photocatalytic performance of diphasic $\text{Ba}_{1-x}\text{Ca}_x\text{TiO}_3$ nanowires near a solubility limit. *Catal. Sci. Technol.* **9**, 6863–6874 (2019).
84. Zhou, X. *et al.* Excellent catalytic performance of molten-salt-synthesized $\text{Bi}_{0.5}\text{Na}_{0.5}\text{TiO}_3$ nanorods by the piezo-phototronic coupling effect. *Nano Energy* **84**, 105936 (2021).
85. Zhang, C. *et al.* pn Heterojunction of BiOI/ZnO nanorod arrays for piezo-photocatalytic degradation of bisphenol A in water. *J. Hazard. Mater.* **399**, 123109 (2020).

Acknowledgements

This work was supported by the Korea Institute of Energy Technology Evaluation and Planning (KETEP) and the Ministry of Trade, Industry & Energy (MOTIE) of the Republic of Korea (No. 20192010106790 and No. 20204010600090). The authors extend their appreciation to the Deanship of Scientific Research at King Khalid University, Saudi Arabia for funding this work through Large Research Groups Program under Grant Number L.R.G.P2/274/44.

Author contributions

M.K. designed the research, conducted the experiments, and prepared the manuscript and rest of the authors R.V., I.K., I.B., H.P., Y.J., T.S. and A.K. have reviewed/edited the manuscript.

Competing interests

The authors declare no competing interests.

Additional information

Supplementary Information The online version contains supplementary material available at <https://doi.org/10.1038/s41598-023-33658-2>.

Correspondence and requests for materials should be addressed to A.K.

Reprints and permissions information is available at www.nature.com/reprints.

Publisher's note Springer Nature remains neutral with regard to jurisdictional claims in published maps and institutional affiliations.



Open Access This article is licensed under a Creative Commons Attribution 4.0 International License, which permits use, sharing, adaptation, distribution and reproduction in any medium or format, as long as you give appropriate credit to the original author(s) and the source, provide a link to the Creative Commons licence, and indicate if changes were made. The images or other third party material in this article are included in the article's Creative Commons licence, unless indicated otherwise in a credit line to the material. If material is not included in the article's Creative Commons licence and your intended use is not permitted by statutory regulation or exceeds the permitted use, you will need to obtain permission directly from the copyright holder. To view a copy of this licence, visit <http://creativecommons.org/licenses/by/4.0/>.

© The Author(s) 2023